PAPER

Check for updates

A highly sensitive gas sensor employing biomorphic SnO₂ with multi-level tubes/pores structure: bio-templated from waste of flax

Xilin Jia,†[a] Ning Wang,†[c] Junlong Tian, [ID] *[a] Yong Zhang,[a] Donglin Lu,[a] Junjiang Tan,[a] Ruyi Qiao,[a] Lulu Chen,[a] Wang Zhang[b] and Jianxin Zhong[a]

Metal oxide gas sensors with porous structures are widely used in numerous applications ranging from health monitoring and medical detection to safety; in this study, we report a highly sensitive SnO₂ gas sensor with a multi-level tube/pore structure prepared *via* biomimetic technology using flax waste as a bio-template and a simple wet chemical process combined with subsequent annealing. Indeed, MLTPS not only maintained and improved the excellence of porous structure gas sensing materials with abundant active sites and large surface-to-volume ratios, but also overcame the deficiency of the lack of gas diffusion channels in porous gas sensing materials. Thus, this novel multi-level tube/pore SnO₂ gas sensor exhibited significantly enhanced sensing performance, *e.g.* an ultra-low response concentration (250 ppb), a high response (87.9), a fast response (9.2 s), a low operating temperature (130 °C) and good stability, for formaldehyde. On the basis of these results, *via* the reuse of agricultural waste, this study provides a new concept for the low-cost synthesis of environmentally friendly and effective multi-level tube/pore gas sensor materials.

1. Introduction

Semiconducting metal oxide-based gas sensors have aroused significant research interest owing to their low cost, easy production and high sensitivity, stability, and scalability.[1–5] They are broadly applied in fields ranging from health monitoring and medical detection to safety.[3,6–8] Among the currently available metal oxide semiconductors, SnO₂, as a typical n-type semiconductor with a 3.6 eV band gap, has been extensively studied in the field of gas sensors and applied to the detection of a number of different gases such as HCHO, CH₃OH, NH₃, C₂H₆O, CO, SO₂, CH₄ and H₂S.[6,9–14] However, the practical applications of SnO₂ have been limited due to its low selectivity, high operating temperature and unsatisfactory sensing response. Recently, to overcome these limits, most efforts to optimize its performance have been based on composition modification, structure optimization and process improvement.[12,15] Obviously, composition modification is

a fundamental optimized route. For example, Yang *et al.* doped Cu and Zn into SnO₂ and obtained a highly sensitive and low-operating temperature gas sensor.[12] Sun *et al.* decorated SnO₂ with CeO₂, which presented enhanced gas sensing properties.[16] Choa *et al.* synthesized $Cu_{x(x=1,2)}O$:SnO₂ thin film nanocomposites, which exhibited a fast response (21 s) and recovery speed.[17] Xu *et al.* decorated SnO₂ with bimetal PdAu, and exhibited dual selectivity for detecting formaldehyde and acetone.[6] However, composition modification faces challenges in terms of control of the component quantity and complicated synthesis processes; this adds to the cost of the materials. Moreover, because the sensing mechanism of SnO₂ is surface-control type, a large number of researchers have made significant efforts to develop novel structures to improve its gas sensing performance.[18] For example, Huang *et al.* prepared porous flower-like SnO₂ nanostructures that exhibited good response and reversibility to some organic vapors.[18] Liu *et al.* synthesized hierarchical meso-macroporous SnO₂ that exhibited higher gas response in the detection of indoor air pollutants.[19] Wang *et al.* synthesized 3D hierarchical SnO₂ nanostructure sensors that exhibited excellent gas sensing performance.[13] Kim *et al.* easily synthesized Pt-functionalized meso/macroporous SnO₂ hollow spheres with outstanding response and selectivity toward H₂S at 250 °C.[20] In particular, among diverse morphologies and structures, porous structures have attracted substantial research interest due to their abundant active sites and large surface-to-volume ratios. However, porous structures lack gas diffusion channels for gas sensing.[19]

[a]Hunan Key Laboratory of Micro-Nano Energy Materials and Devices, Laboratory for Quantum Engineering and Micro-Nano Energy Technology, School of Physics and Optoelectronic, Xiangtan University, Hunan 411105, P. R. China. E-mail: jltian666@xtu.ede.cn

[b]State Key Laboratory of Metal Matrix Composites, Shanghai Jiao Tong University, 800 Dongchuan Road, Shanghai 200240, P. R. China

[c]Institute of Advanced Materials (IAM), Jiangsu National Synergistic Innovation Center for Advanced Materials (SICAM), Nanjing Tech University (Nanjing Tech), 30 South Puzhu Road, Nanjing 211816, P. R. China

† Xilin Jia and Ning Wang contributed equally to this work.

However, due to the limits of the chemical synthesis process, it is difficult to prepare optimized and complex fine structures to further improve gas sensing performance. To overcome this challenge, in our previous work, we combined chemosynthesis with biomimetic techniques to fabricate SnO_2 tubes with hollow and porous structures on their walls which exhibited high gas sensitivity.[9,10]

Among the above-discussed detection gases, HCHO is one of the most common harmful gases among volatile organic compounds that appear in indoor pollutants and the food industry; it causes multifarious diseases and was classified as a human carcinogen by the World Health Organization (WHO) in 2017.[21,22] Furthermore, due to the different HCHO content levels in the exhaled breath of healthy humans (48 ppb) and lung cancer patients (83 ppb), HCHO has been proposed to be a biomarker for lung cancer detection.[8,23,24] Therefore, the detection of HCHO is necessary, and its great significance has aroused wide interest. However, most semiconducting metal oxide-based HCHO sensors still contain defects. For example, they generally demand higher operating temperatures, from 200 °C to 600 °C,[22,25–27] and show low selectivity.[26–28]

In order to avoid the challenges of composition modification and overcome the limits of structure optimization, in this work, we combined chemosynthesis with biomimetic techniques to fabricate novel multi-level tubes/pores SnO_2 (MLTPS). Herein, we used low-cost agricultural flax waste as a sacrificial template. Compared with traditional SnO_2 nanomaterials, MLTPS not only shows abundant active sites and a large surface-to-volume ratio but also possesses effective gas diffusion channels, which exhibit better HCHO response and lower operating temperatures. Consequently, this work provides new insight to fabricate high-performance and low cost HCHO gas sensors.

2. Experimental

2.1. Preparation of MLTPS

In this work, combining chemosynthesis with biomimetic techniques, MLTPS was fabricated using a modified method in our previous work.[9,10,29] Fig. 1 shows the strategy employed for fabricating MLTPS. Herein, flax waste, which possesses multi-level tubes/pores structures, was chosen as a bio-template. The fabrication route consists of three steps. First, flax waste was cut into cylindrical pieces. The length of these cylinders was about 1 cm and their diameter was about 0.2 cm. Next, to aminate the flax waste cylinders, the cylinders were heated in 5% dilute ammonia at 100 °C for 10 h, then washed in deionized water and dried in air at 70 °C for 8 h. In the second step,

the pretreated cylinders were dipped into a prepared $SnCl_2$ ethanol solution ($SnCl_2$ 0.65 g, 30 ml of ethanol solution with a volume fraction of 65%, stirred for 8 h at 25 °C) for 36 h at 40 °C in a sealed vessel, rinsed with deionized water and dried in air for 12 h at 70 °C. Lastly, they were sintered in a tube furnace at a rate of 1 °C min^{-1} to 550 °C and maintained for 2 h (the hemicellulose, cellulose and lignin were burnt off, and crystallized SnO_2 remained). Then, the SnO_2 cylinders were cooled to room temperature and MLTPS was obtained.

2.2. Characterization

MLTPS was characterized by X-ray diffraction (XRD, Ultima IV, Cu K radiation, $\lambda = 0.15406$ nm, 40 kV, 400 mA). The microstructure and morphology of MLTPS were observed by scanning electron microscopy (SEM, VEGA3SBH, JSM-IT300) operated at 20 kV. The transmission electron microscopy (TEM) images, high resolution transmission electron microscope (HRTEM) images and selected area electron diffraction (SAED) patterns were obtained on a Tecnai G2 F20 S-TWIN TMP instrument operated at an acceleration voltage of 200 kV. The gas sensing performance of MLTPS was studied on a CGS-8 intelligent gas sensing system (resistive type) (Beijing Elite Tech Co., Ltd.). N_2 adsorption measurements were taken with an ASAP2460 Autosorb-iQ2-MP adsorption analyzer, and the pore size distributions (PSD) of the samples were calculated using the BJH algorithm.

2.3. Fabrication of the gas sensor and the gas sensing measurement system

The fabrication process of the gas sensor was as follows: first, the as-prepared MLTPS was mixed with terpineol to form a homogeneous paste. Then, using a small brush, the homogeneous paste was coated on a ceramic tube attached to a pair of gold electrodes to form a thin film. Next, the coated ceramic tube was dried at 60 °C for 24 h. Furthermore, a Ni–Cr alloy coil was inserted into the ceramic tube to form a heating resistor, which provided the operating temperature of the gas sensor. The operating temperature was controlled by tuning the heating current. In the last step, in order to improve the long-term stability of the as-prepared gas sensor, the aging process of the sensor was performed for 2 h on a gas sensitivity instrument (Beijing Elite Tech Co., Ltd.).

The sensing measurements were performed using a CGS-8 intelligent gas sensing system (resistive type) (Beijing Elite Tech Co., Ltd.) under laboratory conditions (30 RH%, 25 °C). Herein, a static system was used to test the gas response, where
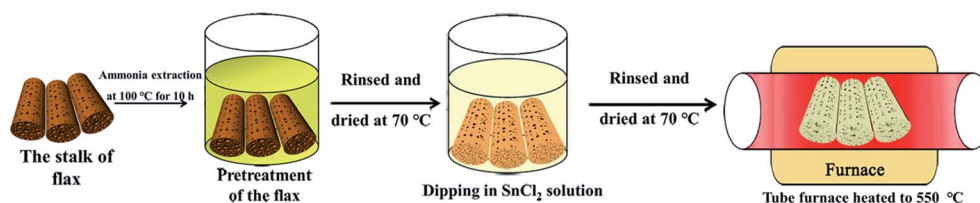

Fig. 1 Schematic of the preparation of MLTPS.

the target gas was induced by injecting its corresponding liquid and vaporizing it by a heater. The gas response (S) of the sensor in this paper was defined as the resistance ratio R_a/R_g, where R_a is the resistance in air and R_g is the resistance in air mixed with the tested gas. The response or recovery time was expressed as the time needed for the sensor output to reach 90% saturation after switching off the gas in a step function.

3. Results and discussion

3.1. Characterization of MLTPS

In this work, combining a simple and low cost chemosynthesis method with biomimetic techniques, biologically novel multi-level tubes/pores SnO_2 (MLTPS) was obtained. The morphology and structure of MLTPS are shown in Fig. 2 and 3. From the SEM images of MLTPS (Fig. 2), the multi-level tube array and pore morphology can be observed. As shown in Fig. 2(a), MLTPS preserved the multi-tubular pore array from the flax waste, and the diameter of these multi-tubular pores ranges from approximately 2 μm to 3 μm. In addition, pores are regularly distributed on the walls of the multi-tubular pores array (Fig. 2(b)–(e)), and the average diameter of these pores is about 2 μm. It is clear that the multi-tubular array and pores formed a hierarchically multi-level tubes/pores structure. The multi-level tube array and pores structure shows excellent performance for gas diffusion and successfully overcame the deficiency of porous structures which lack gas diffusion channels. Moreover, in order to further confirm the hierarchically multi-level tubes/pores structure, TEM observations were used. Fig. 3(a)–(c) also show the morphology of the multi-tubular and porous walls. The high-magnification TEM images (Fig. 3(b)–(d)) indicate that the multi-level tubes/pores structure consists

of interconnected nanoparticles with an average diameter of about 7.39 nm. Nanoparticles spontaneously aligned with one another and attached to the surface of the multi-tubular walls to form a porous sponge-like multi-level tubes/pores structure with interior cavities and loose structures, which is beneficial to inward and outward gas diffusion and gas sensing.[28,30] Consequently, for gas sensors, MLTPS not only has abundant active sites and a large surface-to-volume ratio, but also possesses numerous diffusion channels.

The HRTEM images of MLTPS (Fig. 3(d)) evidently show that the interconnected nanoparticles that form the loose structures are SnO_2 nanoparticles. The lattice fringes have interplanar distances of $d_{SnO_2}(101) = 0.264$ nm and $d_{SnO_2}(110) = 0.343$ nm (Fig. 3(d)). From Fig. 3(e), it can be seen that the SAED image is a typical SnO_2 polycrystallinity diffraction pattern, and the rings can be indexed to the (110), (101), (200), (220) and (310) crystal planes, respectively. The XRD result is shown in Fig. 3(f). The XRD pattern shows that the diffraction peak of MLTPS corresponds to the standard SnO_2 PDF card (#41-1445), which demonstrates that the nanoparticles are tetragonal phase SnO_2. The lattice plane corresponding to the diffraction peak has been marked in the image (Fig. 3(f)). The clear rings of the SAED image (Fig. 3(e)) match well with the XRD result (Fig. 3(f)).

The chemical states and elemental composition of MLTPS were determined by XPS. Fig. 4 shows the typical XPS spectra. The survey spectrum (Fig. 4(a)) indicates that MLTPS consists of Sn and O elements.[31] As shown in Fig. 4(b), the peaks in the Sn 3d spectrum located at 486.63 eV and 495.03 eV originate from the Sn $3d_{5/2}$ and Sn $3d_{3/2}$ core level states, respectively.[30] The values correspond to the binding energies of Sn^{4+} ion.[27] The O 1s high resolution XPS spectrum is shown in Fig. 4(c). As shown in Fig. 4(c), the O 1s peak is asymmetric, and the broadened
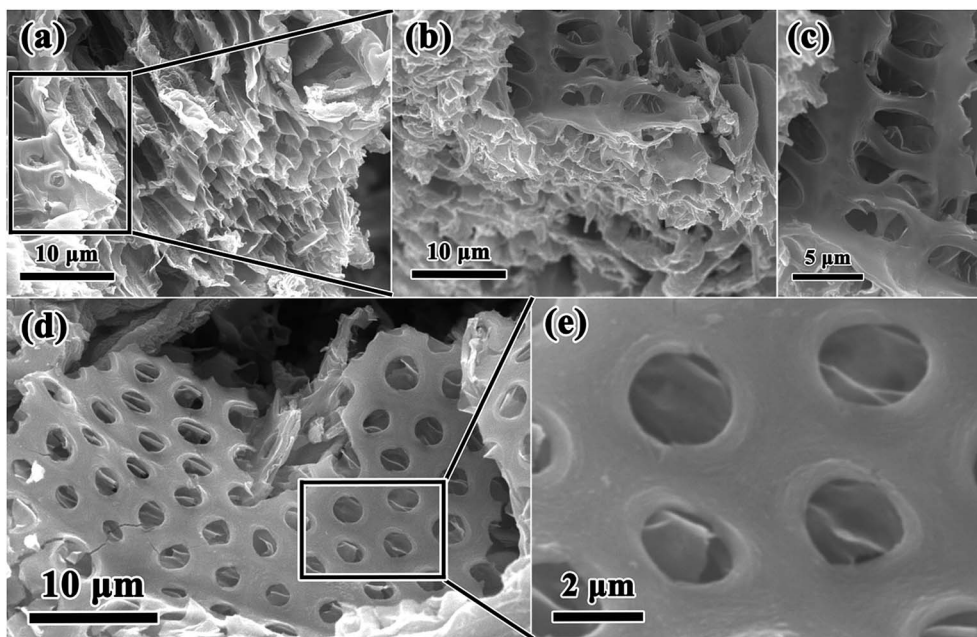

Fig. 2 SEM images of the tubes/pores structure of MLTPS. (a) Cross section image of MLTPS, (b) large field image of the rectangular area in (a), (c) magnified image of the figure in (b), (d) image of the porous structure of MLTPS and (e) magnified image of the selection in (d).
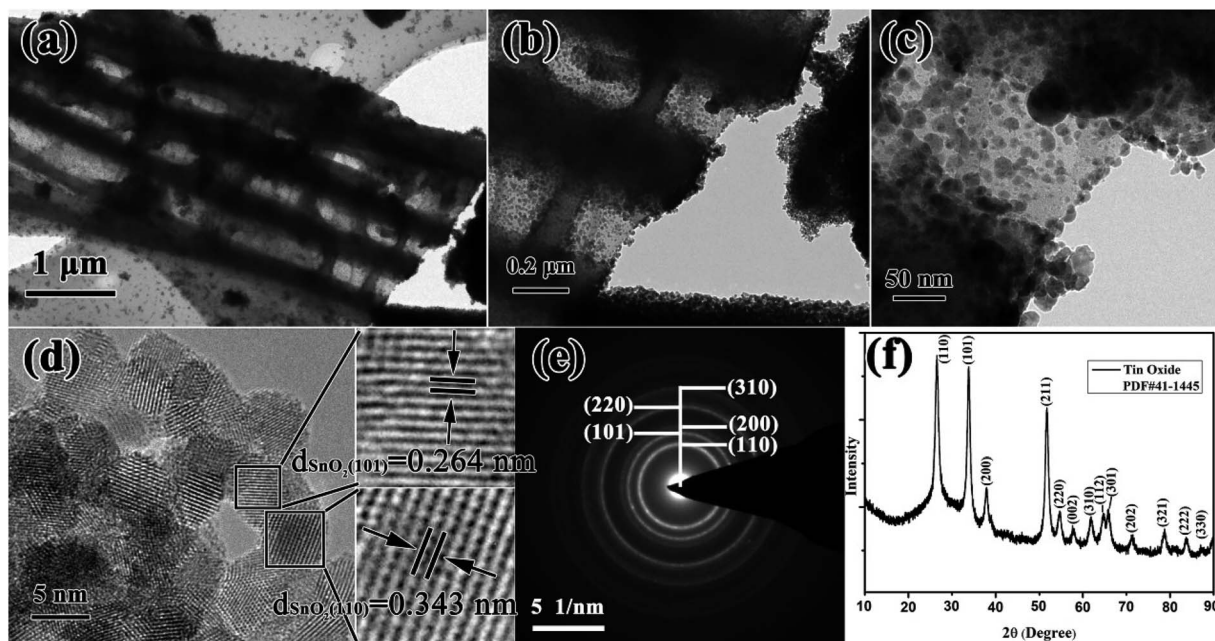
Fig. 3 (a)–(c) TEM images of the MLTPS tubes/pores structure, (d) HRTEM image of MLTPS, (e) SAED image of MLTPS, (f) XRD pattern of MLTPS.

peak can be Gaussian divided into two sub-peaks centered at 530.48 eV and 531.89 eV, respectively. The low binding energy (530.48 eV) can be assigned to the lattice O^{2-} ions in the SnO_2 species. The high binding energy (531.89 eV) is usually attributed to the oxygen species of O^- and O^{2-} absorbed on MLTPS.[30] The chemisorbed oxygen species play an important role in gas sensing performance. Therefore, greater amounts of absorbed oxygen species contribute to greater improvement of the gas sensing properties.[32]

The architecture of the microporous and mesoporous structures of MLTPS was determined by nitrogen adsorption and desorption measurements. The nitrogen adsorption and desorption isotherms curve of MLTPS, the BJH adsorption cumulative pore volume and MLTPS pore size distribution (PSD) plot (inset) are shown in Fig. 5. MLTPS showed an obvious hysteresis loop (Fig. 5(a)), and the hysteresis loop was not steep; this indicates the existence of the multi-level tubes/pores structure.[30] This result was consistent with the SEM and TEM images (Fig. 2 and 3), where the multi-level tube array and pores morphology can be observed. The tubes form gas diffusion channels, which contribute to the transmission of gas. According to the BET surface area plot (inset Fig. 5(a)), the BET surface area of MLTPS is 41.2129 m^2 g^{-1}. Fig. 5(b) shows that the BJH adsorption cumulative volume of the pores is 0.166639 cm^3 g^{-1}. Moreover, the pore size distribution (PSD) curve of biological SnO_2 (inset Fig. 5(b)) demonstrates that the biological SnO_2 possesses a hierarchical pore structure in which the pore size is distributed between 1.78 nm and 168.97 nm and most of the pores have pore sizes of 3.7 nm to 20 nm. This is consistent with the porous sponge-like multi-level tubes/pores structure with interior cavities and loose structures which is shown in Fig. 2 and 3. In conclusion, these results prove that the MLTPS not only possesses abundant active sites and a large surface-to-volume ratio, but also contains numerous gas diffusion channels; these greatly improve the gas adsorption, gas sensing reactions, gas desorption and transport of gas.

3.2. Gas sensing measurements

It is known that the gas response of a semiconductor sensor is usually dependent on the operating temperature. However, as
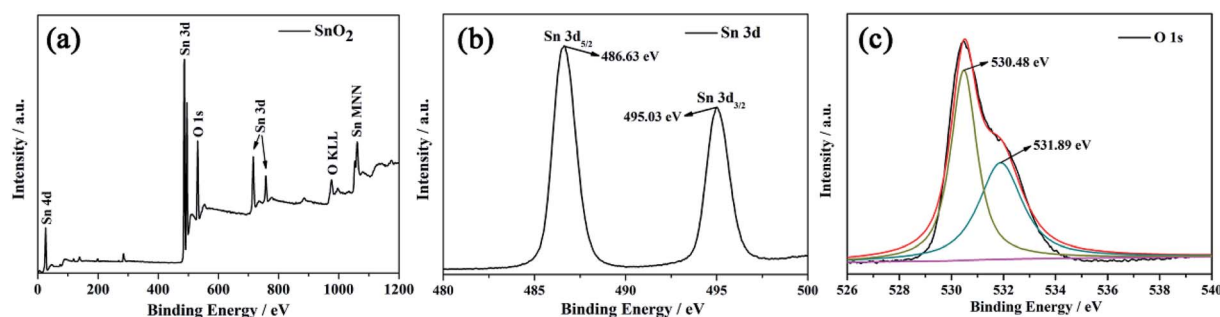

Fig. 4 XPS images of MLTPS. (a) Survey spectrum of multi-level tubes/pores SnO_2 (MLTPS), (b) Sn 3d high resolution XPS spectrum, (c) O 1s high resolution XPS spectrum.
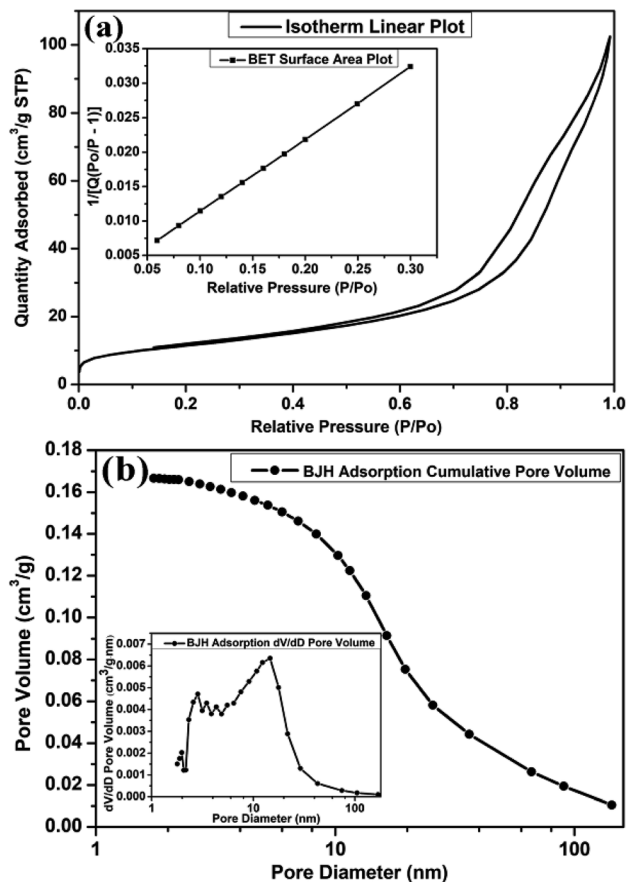
Fig. 5 (a) The nitrogen adsorption and desorption isotherm curves of MLTPS, inset: BET surface area plot, (b) BJH adsorption cumulative pore volume, inset: MLTPS pore size distribution plot.

a typical gas sensing material, pure SnO_2 with a wide band gap (3.6 eV) has a higher operating temperature, which restricts its application for gas detection.[22,25–27] Therefore, the optimal operation temperature of a sensor for detecting gases is significant. In this work, it can be observed in Fig. 6(a) that for HCHO detection, the response increased with operating temperature until it reached a maximum at 130 °C; this may occur because as the operating temperature increases, more oxygen molecules are adsorbed by the material and are

activated to $O_x^{\delta-}$ ($O_x^{\delta-} = O_2^-$, O^-).[6,33,34] The response then decreased rapidly with further increase of the operating temperature, which may occur because large amounts of reactants were desorbed.[6,33] Therefore, 130 °C is the optimal operating temperature of the MLTPS sensor; this optimal operating temperature is obviously lower than those in numerous reported studies (higher operating temperatures from 200 °C to 600 °C).[22,25–27] Here, the low operating temperature (130 °C) is due to the fact that MLTPS has abundant active sites, a large surface-to-volume ratio and numerous gas diffusion channels, which results in a faster adsorption/desorption rate. Reasonably, the subsequent gas sensing measurements were conducted at the optimal operating temperature (130 °C). Gas sensing repeatability is an important parameter to evaluate the sensing ability of semiconductor materials. Here, the repeatability of the MLTPS gas sensor was studied by testing the changes in the resistance response sensitivity to 50 ppm HCHO with time at 130 °C in three continuous test cycles. From Fig. 6(b), it can be seen that the response and recovery curves showed negligible changes in the continuous test cycles. The reproducibility tests demonstrate that MLTPS has excellent reversibility and repeatability for HCHO detection.

In order to study the response and recovery characteristics of MLTPS, this work analysed the response and recovery times of MLTPS to 50 ppm HCHO at 130 °C. As shown in Fig. 6(c), the response time and recovery time of MLTPS are 9.2 s and 151.0 s, respectively. The quick response time (9.2 s) is faster than those in previously reported work.[26,35,36] The quick response and recovery can be attributed to the numerous gas diffusion channels of MLTPS, which enable rapid adsorption, desorption and gas diffusion.

The compositions of indoor home gas and human exhaled breath are complicated. Hence, selectivity is of great importance to practical applications, such as indoor toxic gas detection and biomarkers.[6] Here, in order to clarify its potential gas sensing applications for indoor toxic gas detection and biomarkers, the selectivity of the MLTPS gas sensor was tested with 50 ppm potential interference gases (ammonia (NH_3), methanol (CH_3OH), ethanol (C_2H_6O) and formaldehyde (HCHO)) at 130 °C. These gases are typical components of indoor toxic gas and biomarkers. The selectivity of the MLTPS gas sensor to 50 ppm of the abovementioned gases at 130 °C is displayed in
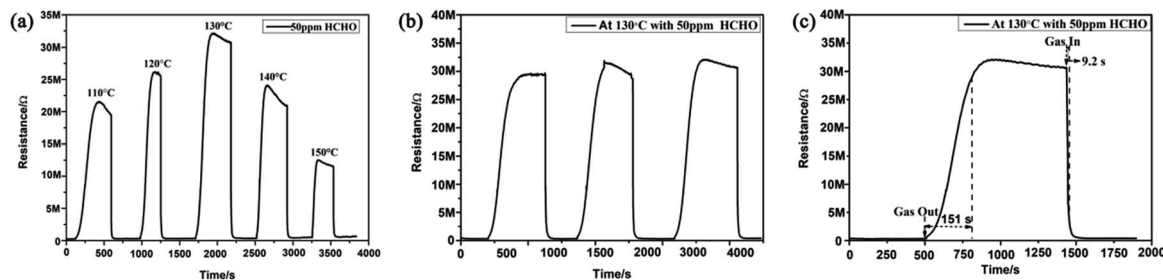

Fig. 6 (a) Response and recovery curves of MLTPS to 50 ppm HCHO at different operating temperatures, (b) repeatability of MLTPS for sensing 50 ppm HCHO at 130 °C. Resistance response sensitivity changes with time in three continuous test cycles. (c) Response and recovery characteristics of MLTPS to 50 ppm HCHO at the operating temperature of 130 °C.

Fig. 7. From Fig. 7(a), it can be found that the MLTPS gas sensor showed obviously high response and excellent sensitivity to HCHO, whereas it exhibited relatively low responses to CH_3OH, C_2H_6O and NH_3 under the same test conditions. As demonstrated in Fig. 7(b), the response of the MLTPS gas sensor to HCHO is the highest (87.9); meanwhile, the responses to CH_3OH, C_2H_6O and NH_3 are 17.6, 5.5 and 1.3, respectively. The response to HCHO was about 5.0, 16.0 and 67.6 times higher than the responses to CH_3OH, C_2H_6O and NH_3, respectively. Consequently, the MLTPS gas sensor showed excellent selectivity to HCHO, which is one of the most common harmful gases among volatile organic compounds appearing in indoor pollutants and the food industry and is also a biomarker for lung cancer detection. The mechanism of high HCHO selectivity can be explained through the following two aspects. As one reason, the molecular structures and bond dissociation energies are significant influences. As shown in Table 1, the HCHO band energy is smaller than those of other gases at a lower temperature, where it is only 364.0 kJ mol^{-1}. The smaller band energy of HCHO can be broken more easily to realize the reaction between the gas molecules and the sensing material during chemical absorption. On the other hand, the effective diffusion is another important factor. In addition to

Table 1 Target gas bonds and bond energies[37]

Gas type	NH_3	CH_3OH	C_2H_6O	HCHO
Bond	$H–NH_2$	$H–OCH_3$	$H-OC_2H_5$	$H–CHO$
		$H–CH_2$	$H–CH_2$	
		$H–CH$	$H–CH$	
Bond energy (kJ mol^{-1})	435.0	436.8	436.0	364.0
		473.0	473.0	
		452.0	452.0	

the pore size distribution and surface area, it is deduced that Knudsen diffusion will play a key role in the gas diffusion during the sensor process, according to the classic mean free paths (MFP) of the gas molecule formula:

$$\bar{\lambda} = k_B T \left/ \sqrt{2}\pi d^2\, p \right. \tag{1}$$

where k_B is the Boltzmann constant in J K^{-1}, T is the temperature in K, p is the pressure in Pascals, and d is the diameter of the gas particles in meters.

The MFP values of the four target gases (HCHO, CH_3OH, C_2H_6O and NH_3) were estimated as 36.56 nm,[38] 139.00 nm,[39] 25.39 nm,[38] and 46.37 nm,[38] respectively. Because the MFP values of the four target gases are far less than the diameters of the multi-tubular pores array, molecular diffusion was the main diffusion method when the target gas first began to diffuse into the MLTPS. When the target gases diffused into a deeper area inside the MLTPS, the MFP values of the four target gases were larger than average pore size (12.95 nm) of MLTPS; at this time, Knudsen diffusion played a key role in the gas diffusion during the sensing process. The diffusion coefficient D_k is shown in eqn (2):

$$D_k = \frac{4r}{3}\sqrt{(2RT/\pi M)} \tag{2}$$

where r is the pore width, R and T are the universal gas constant and temperature, respectively, and M is the molecular mass of the gas molecule. In fact, compared with CH_3OH and C_2H_6O, the molecular mass of HCHO is smaller. Therefore, the diffusion coefficient of HCHO is higher, which will result in a better response. However, although the molecular mass of NH_3 is smaller than the molecular mass of HCHO and, thus, the diffusion coefficient of NH_3 is higher, the band energy of NH_3 is much higher than that of HCHO; thus, the reaction between the gas molecules and the sensing material during chemical absorption is more difficult. Consequently, at low temperature, the MLTPS gas sensor showed excellent selectivity to HCHO.

Furthermore, this work examined the response of the MLTPS gas sensor to three different HCHO gas concentrations ranging from 250 ppb to 1000 ppb at the optimum working temperature (130 °C). Fig. 8 shows the dynamic response curve and the relationship between the response sensitivity and gas concentration to low HCHO concentrations (250 to 1000 ppb) at 130 °C. As shown in Fig. 8(a), the dynamic response–recovery curve of the MLTPS gas sensor obviously changed stepwise upon exposure of the gas sensor to different concentrations of HCHO, which also illustrates that the MLTPS gas sensor exhibits
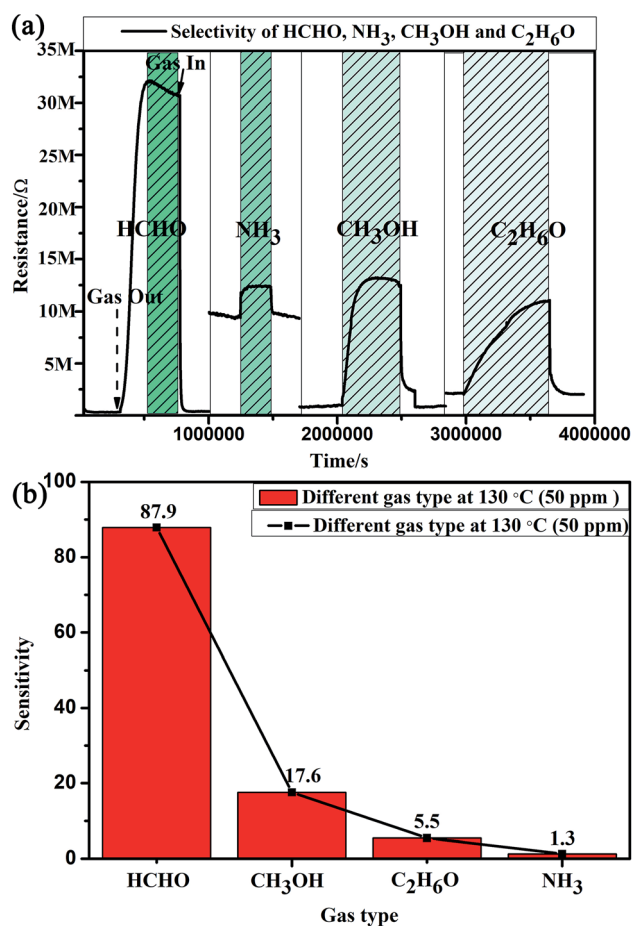

Fig. 7 Selectivity of the MLTPS gas sensor to 50 ppm HCHO, CH_3OH, C_2H_6O and NH_3 at 130 °C. (a) The response and recovery curves of the different gases. (b) The responses of MLTPS to different gases.
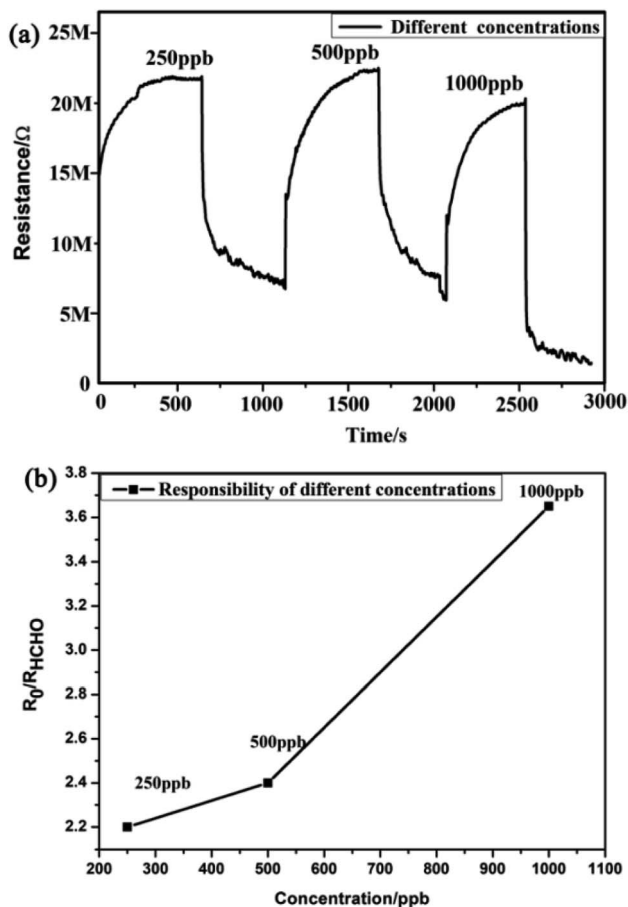
Fig. 8 The gas sensing properties of the sensor based on MLTPS at an operating temperature of 130 °C. (a) The dynamic response curve of the MLTPS gas sensor to low HCHO concentrations (250 to 1000 ppb). (b) The relationship between response sensitivity and gas concentration.
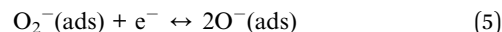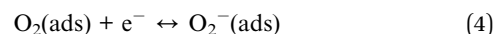
excellent reliability even upon exposure to low gas concentrations. Also, the corresponding responses of the MLTPS gas sensor gradually increased with increasing concentration of HCHO from 250 ppb to 1000 ppb (Fig. 8(b)). The responses of the MLTPS gas sensor to the low HCHO concentrations (250 ppb, 500 ppb and 1000 ppb) at 130 °C were 2.20, 2.40 and 3.65, respectively. Consequently, these results demonstrate that the MLTPS gas sensor is reliable and exhibits excellent response even upon exposure to low gas concentrations (250 to 1000 ppb), which is suitable for potential gas sensing applications for indoor toxic gas and biomarker detection.

Here, Table 2 shows a comparison of the HCHO gas sensitivity performance of nanostructured materials (based on SnO_2) with different structures. As shown in Table 2, the sensor in this work (SnO_2 (biomorphic MLTPS)) exhibited a higher response value (87.9/50 ppm) than other HCHO gas sensors containing a single SnO_2 component,[26,36] decorated SnO_2,[35,40–42] and composite SnO_2.[43] In addition, while fast response and recovery times (2 s/7 s) were reported, their operating temperatures were higher than that of the MLTPS gas sensor. Compared with the operating temperatures of these HCHO gas sensors (160 °C to 300 °C), the operating temperature of the MLTPS gas sensor is
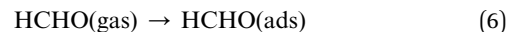
lower (130 °C). In brief, although it contains a single SnO_2 component, the MLTPS gas sensor exhibits excellent response and fast response/recovery times at a low operating temperature; this indicates that the MLTPS gas sensor is a promising HCHO sensor for indoor toxic gas detection and biomarkers.

3.3. Sensing mechanism

Furthermore, here, the gas sensing mechanism of MLTPS is discussed from the following aspects. On one hand, SnO_2 is one of the most representative n-type oxide semiconductor gas sensing materials. The sensor mechanism of SnO_2 is explained as a change in electrical conductivity which is caused by the chemical interaction of gas molecules with the surface of the gas sensor material.[44] In this mechanism, the electrical conductivity change of MLTPS is related to the amount and species of chemisorbed oxygen during the adsorption and desorption processes. Firstly, when the MLTPS sensor is exposed to air, oxygen molecules can be absorbed on the surface of MLTPS by capturing electrons from the conduction band of SnO_2 to form chemisorbed oxygen ions; this decreases the concentration of electrons, which results in increased resistance and decreased electrical conduction (Fig. 9).[6,26] In this work, the optimal operating temperature of MLTPS was 130 °C. At low operating temperatures (<200 °C),[34,45] the chemisorbed oxygen ion process can be expressed as follows:[26]

$$O_2(gas) \leftrightarrow O_2(ads) \tag{3}$$

$$O_2(ads) + e^- \leftrightarrow O_2^-(ads) \tag{4}$$

$$O_2^-(ads) + e^- \leftrightarrow 2O^-(ads) \tag{5}$$

Then, when the MLTPS gas sensor is exposed to HCHO, which is a reducing gas, the gas molecules react with the adsorbed oxygen ions and release the trapped electrons back to the conduction band of the SnO_2 gas sensing material, leading to decreased thickness of the space-charge layer and potential barrier, as shown in Fig. 9.[26,30] Finally, it was shown that the resistance of the MLTPS gas sensor decreases and the electrical conduction increases. The process by which formaldehyde gas molecules are adsorbed onto the surface of MLTPS and react with $O_x^{\delta-}$ ($O_x^{\delta-} = O_2^-$, O^-) can be expressed as follows:[46,47]

$$HCHO(gas) \rightarrow HCHO(ads) \tag{6}$$

$$HCHO(ads) + O_2^-(ads) \rightarrow CO_2(gas) + H_2O + e^- \tag{7}$$

$$HCHO(ads) + 2O^-(ads) \rightarrow CO_2(gas) + H_2O(gas) + 2e^- \tag{8}$$

On another hand, as shown in Fig. 2 and 9, the gas molecules absorbed on the surface of the porous sponge-like multi-level tubes/pores structure of MLTPS and reacted with SnO_2 nanoparticles. Then, the gas molecules diffused effectively in the multi-tubular structures of MLTPS.

Consequently, the excellent gas sensing performance to HCHO exhibited by MLTPS can be explained in two aspects. In one respect, its excellent gas sensing performance can be

Table 2 Comparison of the formaldehyde gas sensitivity performance of nanostructured materials with different structures

| Response material (material structure)	Response/recovery times (s)	Operating temperature (°C)	Sensor response (S)/target gas concentration (ppm)
SnO_2 (microspheres)	17.0 s/25.0 s (100 ppm)	200 °C	38.3/100 ppm (ref. 26)
SnO_2 (hollow microspheres)	30.0 s/30.0 s (200 ppm)	300 °C	9.0/200 ppm (ref. 36)
Sb-doped SnO_2 (hierarchical peony-like)	10.0 s/20.0 s (10 ppm)	280 °C	30.0/50 ppm (ref. 40)
In/Pd–SnO_2 (microspheres)	5.0 s/— (100 ppm)	160 °C	24.6/100 ppm (ref. 41)
NiO-doped SnO_2 (nanofibers)	50.0 s/80.0 s (10 ppm)	200 °C	14.0/50 ppm (ref. 35)
Pd decorated SnO_2 (nanofibers)	2 s/7 s (100 ppm)	160 °C	24.0/1000 ppm (ref. 42)
NiO/SnO_2 (microspheres)	5.0 s/15.0 s (50 ppm)	240 °C	27.6/100 ppm (ref. 43)
SnO_2 (biomorphic MLTPS)	9.2 s/151.0 s (50 ppm)	130 °C	87.9/50 ppm (this work)
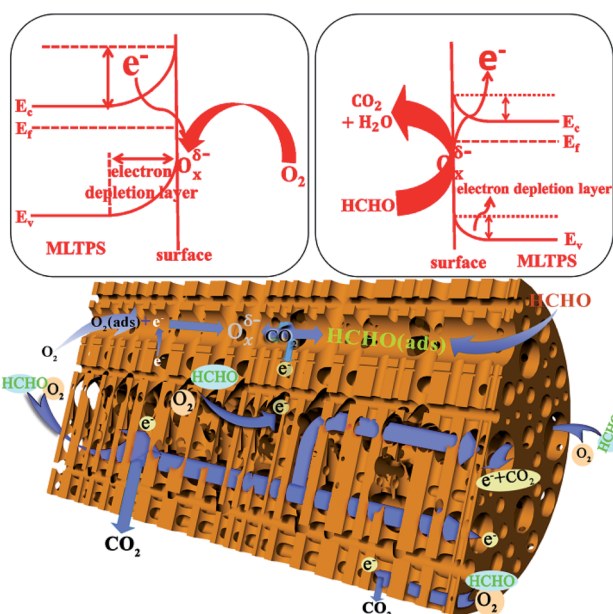
Fig. 9 Schematic of the gas sensing mechanism.

attributed to the porous sponge-like multi-level tubes/pores structure with interior cavities and loose structures. Firstly, its porous sponge-like multi-level tubes/pores structure showed a large specific surface area (41.2129 m² g⁻¹) and abundant active sites which can supply an adequate surface for absorbing and sensing reactions of gas molecules. Secondly, the interconnected multi-tubular structure provided numerous gas diffusion channels; thus, the gas diffusion was more effective. Indeed, MLTPS not only maintained and improved the performance of porous structure gas sensing materials with abundant active sites and large surface-to-volume ratios, but also overcame the deficiency of the lack of gas diffusion channels in porous structure gas sensing materials. Thus, MLTPS exhibited high HCHO response, fast response–recovery characteristics and low gas concentration response at a low operating temperature. In another aspect, the excellent gas sensing performance of MLTPS can be attributed to the suitable grain sizes of its SnO_2 nanoparticles. Because the response and recovery processes are controlled by the surface-charge model, when the grain size is decreased to a scale comparable to the thickness of the surface electron depletion layer (L_d), the gas

sensing performance can be highly enhanced.[26,48] Compared with the L_d (about 3 nm) for SnO_2 materials in air,[26] the average SnO_2 grain size of MLTPS (about 7.39 nm) was close to $2L_d$. This indicates that the almost full depletion of electrons promoted the action rate between chemisorbed oxygen ions with HCHO molecules, which improved the response of the sensing materials.

4. Conclusions

In summary, MLTPS with a multi-level tubes/pores structure was successfully prepared by combining facile and low cost chemosynthesis with biomimetic techniques. The SnO_2 nanoparticles spontaneously aligned with each other and attached to the surface of the multi-tubular walls to form a porous sponge-like multi-level tubes/pores structure with interior cavities and loose structures. Moreover, MLTPS exhibited remarkably enhanced sensing performance to formaldehyde, e.g. ultra-low response concentration (250 ppb), high response (87.9), fast response (9.2 s), low operating temperature (130 °C) and good stability. Indeed, MLTPS not only persisted and improved the excellence of porous structure gas sensing materials with abundant active sites and large surface-to-volume ratios, but also overcame the deficiency of the lack of gas diffusion channels in porous structure gas sensing materials. In conclusion, this work introduced a facile, low-cost and environmentally friendly way to prepare porous gas sensing materials with multi-level tube arrays for effective diffusion channels. Furthermore, this work presented a promising HCHO sensor with great potential for indoor toxic gas detection and biomarkers.

Conflicts of interest

There are no conflicts to declare.

Acknowledgements

References

1 A. A. Abokifa, K. Haddad, J. Fortner, C. S. Lo and P. Biswas, *J. Mater. Chem. A*, 2018, **6**, 2053–2066.

2 Z. Song, Z. Wei, B. Wang, Z. Luo, S. Xu, W. Zhang, H. Yu, M. Li, Z. Huang, J. Zang, F. Yi and H. Liu, *Chem. Mater.*, 2016, **28**, 1205–1212.

3 D. R. Miller, S. A. Akbar and P. A. Morris, *Sens. Actuators, B*, 2014, **204**, 250–272.

4 A. Dey, *Mater. Sci. Eng., B*, 2018, **229**, 206–217.

5 B. Jiang, Y. Zhang, X. Zheng, P. Li, M. Yuan and S. Deng, *Sens. Lett.*, 2015, **13**, 872–877.

6 G. Li, Z. Cheng, Q. Xiang, L. Yan, X. Wang and J. Xu, *Sens. Actuators, B*, 2019, **283**, 590–601.

7 L. Wang, Z. Wang, Q. Xiang, Y. Chen, Z. Duan and J. Xu, *Sens. Actuators, B*, 2017, **248**, 820–828.

8 A. T. Güntner, V. Koren, K. Chikkadi, M. Righettoni and S. E. Pratsinis, *ACS Sens.*, 2016, **1**, 528–535.

9 W. Zhang, J. Tian, Y. a. Wang, X. Fang, Y. Huang, W. Chen, Q. Liu and D. Zhang, *J. Mater. Chem. A*, 2014, **2**, 4543–4550.

10 J. Tian, F. Pan, R. Xue, W. Zhang, X. Fang, Q. Liu, Y. Wang, Z. Zhang and D. Zhang, *Dalton Trans.*, 2015, **44**, 7911–7916.

11 J. Guo, J. Zhang, H. Gong, D. Ju and B. Cao, *Sens. Actuators, B*, 2016, **226**, 266–272.

12 W. Zhang, B. Yang, J. Liu, X. Chen, X. Wang and C. Yang, *Sens. Actuators, B*, 2017, **243**, 982–989.

13 S. Wang, J. Yang, H. Zhang, Y. Wang, X. Gao, L. Wang and Z. Zhu, *Sens. Actuators, B*, 2015, **207**, 83–89.

14 G. Eranna, B. C. Joshi, D. P. Runthala and R. P. Gupta, *Crit. Rev. Solid State Mater. Sci.*, 2004, **29**, 111–188.

15 R. L. Vander Wal, G. W. Hunter, J. C. Xu, M. J. Kulis, G. M. Berger and T. M. Ticich, *Sens. Actuators, B*, 2009, **138**, 113–119.

16 J. Liu, M. Dai, T. Wang, P. Sun, X. Liang, G. Lu, K. Shimanoe and N. Yamazoe, *ACS Appl. Mater. Interfaces*, 2016, **8**, 6669–6677.

17 N. S. A. Eom, H.-B. Cho, Y. Song, G. M. Go, J. Lee and Y.-H. Choa, *Sens. Actuators, B*, 2018, **273**, 1054–1061.

18 C. Gu, X. Xu, J. Huang, W. Wang, Y. Sun and J. Liu, *Sens. Actuators, B*, 2012, **174**, 31–38.

19 H. Li, F. Meng, J. Liu, Y. Sun, Z. Jin, L. Kong, Y. Hu and J. Liu, *Sens. Actuators, B*, 2012, **166–167**, 519–525.

20 P. M. Bulemo, H.-J. Cho, D.-H. Kim and I.-D. Kim, *ACS Appl. Mater. Interfaces*, 2018, **10**, 18183–18191.

21 Y. Zhang, B. Jiang, M. Yuan, P. Li, W. Li and X. Zheng, *J. Sol-Gel Sci. Technol.*, 2016, **79**, 167–175.

22 L. Xian, W. Jing, X. Dan, X. Jianlong, X. Yi, L. Weiwei, X. Lan, L. Zhemin, X. Shiwei and K. Sridhar, *Nanotechnology*, 2017, **28**, 325501.

23 M. Hakim, Y. Y. Broza, O. Barash, N. Peled, M. Phillips, A. Amann and H. Haick, *Chem. Rev.*, 2012, **112**, 5949–5966.

24 P. Fuchs, C. Loeseken, J. K. Schubert and W. Miekisch, *Int. J. Cancer*, 2010, **126**, 2663–2670.

25 F. Fang, L. Bai, H. Sun, Y. Kuang, X. Sun, T. Shi, D. Song, P. Guo, H. Yang, Z. Zhang, Y. Wang, J. Luo and J. Zhu, *Sens. Actuators, B*, 2015, **206**, 714–720.

26 Y. Li, N. Chen, D. Deng, X. Xing, X. Xiao and Y. Wang, *Sens. Actuators, B*, 2017, **238**, 264–273.

27 C. Gu, Y. Cui, L. Wang, E. Sheng, J.-J. Shim and J. Huang, *Sens. Actuators, B*, 2017, **241**, 298–307.

28 K. Xu, D. Zeng, S. Tian, S. Zhang and C. Xie, *Sens. Actuators, B*, 2014, **190**, 585–592.

29 Z. Liu, T. Fan, J. Ding, D. Zhang, Q. Guo and H. Ogawa, *Ceram. Int.*, 2008, **34**, 69–74.

30 D. Wang, M. Zhang, Z. Chen, H. Li, A. Chen, X. Wang and J. Yang, *Sens. Actuators, B*, 2017, **250**, 533–542.

31 J. Cao, C. Qin, Y. Wang, H. Zhang, B. Zhang, Y. Gong, X. Wang, G. Sun, H. Bala and Z. Zhang, *RSC Adv.*, 2017, 7, 25504–25511.

32 D. Xue, Y. Wang, J. Cao, G. Sun and Z. Zhang, *Talanta*, 2019, **199**, 603–611.

33 R. C. Biswal, *Sens. Actuators, B*, 2011, **157**, 183–188.

34 K. K. Khun, A. Mahajan and R. K. Bedi, *J. Appl. Phys.*, 2009, **106**, 124509.

35 Y. Zheng, J. Wang and P. Yao, *Sens. Actuators, B*, 2011, **156**, 723–730.

36 J. Yang, S. Wang, R. Dong, L. Zhang, Z. Zhu and X. Gao, *Mater. Lett.*, 2016, **184**, 9–12.

37 Z. Liu, T. Fan, D. Zhang, X. Gong and J. Xu, *Sens. Actuators, B*, 2009, **136**, 499–509.

38 W. Zhang, J. Tian, Y. a. Wang, X. Fang, Y. Huang, W. Chen, Q. Liu and D. Zhang, *J. Mater. Chem. A*, 2014, **2**, 4543–4550.

39 D. Mei, M. Qian, B. Liu, B. Jin, Z. Yao and Z. Chen, *J. Power Sources*, 2012, **205**, 367–376.

40 Q. Wei, P. Song, Z. Li, Z. Yang and Q. Wang, *Mater. Lett.*, 2017, **191**, 173–177.

41 Y. Lin, Y. Wang, W. Wei, L. Zhu, S. Wen and S. Ruan, *Ceram. Int.*, 2015, **41**, 7329–7336.

42 Y. Lin, W. Wei, Y. Li, F. Li, J. Zhou, D. Sun, Y. Chen and S. Ruan, *J. Alloys Compd.*, 2015, **651**, 690–698.

43 C. Gu, Y. Cui, L. Wang, E. Sheng, J.-J. Shim and J. Huang, *Sens. Actuators, B*, 2017, **241**, 298–307.

44 H.-J. Kim and J.-H. Lee, *Sens. Actuators, B*, 2014, **192**, 607–627.

45 L. Wang, Z. Lou, R. Zhang, T. Zhou, J. Deng and T. Zhang, *ACS Appl. Mater. Interfaces*, 2016, **8**, 6539–6545.

46 T. Chen, Q. J. Liu, Z. L. Zhou and Y. D. Wang, *Nanotechnology*, 2008, **19**, 095506.

47 Y. Lin, W. Wei, Y. Li, F. Li, J. Zhou, D. Sun, Y. Chen and S. Ruan, *J. Alloys Compd.*, 2015, **651**, 690–698.

48 Y. Zeng, Y. Wang, L. Qiao, Y. Bing, B. Zou and W. Zheng, *Sens. Actuators, B*, 2016, **222**, 354–361.